Modulated heat transfer tube with short conical-mesh inserts: A linking from microflow to macroflow

CrossMark

Zhen Cao, Jinliang Xu *

The Beijing Key Laboratory of Multiphase Flow and Heat Transfer, North China Electric Power University, Beijing 102206, China

ABSTRACT

This paper creates new method that uses microflows through mesh pores to modulate flow and temperature fields. Modulated heat transfer tube (MHTT) was constructed by suspending consecutive conical-mesh inserts in a tube. Because there are too many 3D mesh pores (10–100 μm size) for a conical mesh insert, numerical simulations in laminar flow regime were performed by an 3D to 2D conversion of mesh pores applying equal equivalent diameter criterion and total flow area criterion of mesh pores. The multiscale grid generation linked micron scale of mesh pores and macroscale of the tube. Covering the present data ranges, MHTT had Nusselt numbers which are 1.4–4.1 times of that in a bare tube, PEC (performance evaluation criterion) was up to 2.2, demonstrating excellent heat transfer enhancement at low flow rate pumping cost. The perfect MHTT performance comes from the distinct flow field: an attached hydraulic boundary layer having large velocity and its gradient near the tube wall, a weak circulating flow region upstream of the mesh insert and a weakly positive flow region downstream of the mesh insert. A thin thermal boundary layer on the tube wall was reached to enhance heat transfer. The periodic unit length S and diameter of the conical mesh insert δ were optimized. The varied slopes of Nu versus Re were found and explained while increasing Re. There are best matches of PPI (pores per inch) and Re (Reynolds number). Low PPI mesh insert was suggested at low Re, high PPI mesh insert deformed streamlines to deviate from the perfect flow and temperature fields. Meanwhile, high PPI mesh insert had better performance at high Re. Low PPI mesh insert had good performance, which can be further improved by raising PPI. Because metallic mesh screen is commercialized and cheap, MHTT has wide potential engineering applications.

© 2015 Elsevier Ltd. All rights reserved.

1. Introduction

Heat exchangers are widely used in petrochemical, energy and power industries. Recently, due to the energy shortage and environmental pollution, it is necessary to increase the energy utilization efficiency and decrease the cost of heat exchangers. In the past few decades, many heat transfer enhancement technologies have been developed, including active and passive enhancement technologies. The mechanical agitation, surface vibration, fluid vibration, applied electric and magnetic field belong to the active strategies, while the treated surfaces, rough surfaces, extended surfaces, swirl flow devices and nanofluid are the passive methods [1]. The tube insert is widely used, which is convenient to modify available equipments and clean the fouling. It is also cost-effective. Many researchers worldwide investigated the heat transfer enhancement with tube inserts.

Twisted tape inserts have been applied for a long time. Heat transfer with twisted tape inserts is enhanced by fluid mixing in the main flow region and resisting the boundary layer development near the tube wall. The effects of twisted ratio, pitch, length, width, twisted direction on the heat transfer enhancement were reported in Refs. [2–7]. Kumar & Prasad [2] found the heat transfer coefficients and pressure drops increased by 18–70% and 87–132%, respectively, when twisted ratios were in the range of 3–12. Sarada et al. [3] investigated turbulent heat transfer in a horizontal tube with twisted tape inserts with different widths using air as the working fluid. The heat transfer coefficients were increased by 12% when the widths of twisted tape varied from 10 to 22 mm. Eiamsa-ard et al. [4] found that the higher heat-transfer coefficients and pressure drops were increased with increases in the lengths of twisted tapes. Besides, the winglets were arranged on the surface of staggered/twisted tapes to promote the flow disturbance. It was found that the heat transfer was further improved by raising the contact angle of winglet on the twisted tape surface [5]. Wongcharee and Eiamsa-ard [6] studied the effect of clockwise and

---

* Corresponding author. Tel./fax: +86 10 61772613.
  E-mail address: xjl@ncepu.edu.cn (J. Xu).

Nomenclature

A	flow area of total 3D mesh pore, m^2
A'	flow area of total 2D mesh pore, m^2
BT	bare tube without insert
C_p	specific heat, J/(kg K)
D	tube diameter, m
D_e	equivalent diameter of 3D mesh pores
D'_e	equivalent diameter of 2D mesh pores
EF	heat transfer enhancement factor
MHTT	modulated heat transfer tube with mesh inserts
f	friction factor
g	gravity acceleration ($g = 9.81$), m/s^2
L_1	the distance from the tube entrance to the first conical mesh insert, m
L_2	heat transfer tube length with consecutive mesh inserts, m
m	mass flow rate, kg/s
Nu	average Nusselt number (or called bulk Nusselt number)
Nu_x	local Nusselt number
p	pressure, Pa
Δp	pressure drop in a periodic unit, Pa
PEC	performance evaluation criterion
PPI	pores per inch
q	heat flux, W/m^2
q_w	the heat flux added to the wall, W/m^2
r	radial coordinate, m
Re	Reynolds number
S	periodic unit length, m
T_f	fluid temperature, K
$T_{f,ave}$	average fluid temperature, K
T_{grid}	temperature within the first fluid layer, K
T_{in}	inlet fluid temperature, K

T_{out}	outlet temperature, K
$T_{up.f}$	bulk fluid temperature at inlet, K
T_w	wall temperature, K
$T_{w,ave}$	average wall temperature, K
u	axial velocity, m/s
u_{in}	inlet velocity, m/s
u_{ave}	average velocity, m/s
w	square mesh pore width, m
w'	stripe-type mesh pore width, m
x	axial coordinate, m
y	first fluid layer thickness, m

Greek symbols

α	diverging angle of the conical mesh insert
β	pressure gradient within a periodic unit length, Pa/m
δ	diameter of conical mesh insert at maximum plane, m
η	3D mesh wire thickness, m
η'	2D mesh wire thickness, m
θ	temperature gradient, K/m
λ	thermal conductivity, W/(m K)
μ	dynamic viscosity, Pa s
ρ	density, kg/m^3

Subscript

ave	average
b	bare tube
f	fluid
in	inlet
out	outlet
w	wall
x	axial coordinate

counterclockwise twisted tape inserts on the heat transfer, indicating better performance of staggered axis twisted tape inserts than common inserts. Guo et al. [7] studied effects of the width and hollowing center of twisted tape inserts on the heat transfer, showing the reduced flow resistance by reducing the insert width and increasing the hollowing center area. But, for the tube with narrow twisted tape insert, the heat transfer enhancement is weakened. For the tube with hollowing-center twisted tape insert, the heat transfer is apparently enhanced. There is no fluid mixing in radial direction for laminar flow. The fluid mixing in radial direction is enhanced for turbulent flow. For both flows the thermal resistance comes from the boundary layer thickness. For the tube with twisted tape inserts, heat transfer is enhanced due to strong swirl flow in bulk flow region and enhanced mixing in radial flow direction. Thus, tubes with twist tape inserts are more effective in heat transfer for laminar flow than for turbulent flow. Spiral coil is a new type of insert. Refs. [8,9] experimentally investigated convective heat transfer in tubes with spiral coil inserts in laminar, transition and turbulent flow regions. The performance is better for turbulent flow than that for laminar flow. Pressure loss was mainly influenced by the coil pitch. The smaller the pitch, the greater the pressure loss is. Promvonge [10] studied the heat transfer by inserting coils and twisted tapes in tubes, showing obvious heat transfer enhancement at low Reynolds numbers. Other tube inserts such as ribs, conical nozzle and vortex generator show better heat transfer performance in turbulent flow region [11–13].

It is known that the key issue related to convective heat transfer in tubes is the low velocity and velocity gradient near the tube wall. Cao et al. [14] proposed the flow field modulation concept using a porous mesh membrane insert, dividing the tube cross section into an annular region and a core region. Numerical simulation was performed in laminar flow regime at constant heat flux boundary condition with water as the working fluid. The results show double-peak velocity distribution over tube cross section. The near wall region has larger velocity and velocity gradient, accounting for the heat transfer enhancement mechanism. For a given Reynolds number, there is a critical length beyond which heat transfer is deteriorated. Thus, short mesh membrane inserts were recommended in the tube, ensuring significant heat transfer enhancement over the whole tube length. Xing et al. [15] experimentally studied forced convective heat transfer in tubes with porous mesh membrane insert. Constant heat flux boundary condition was applied with water as the working fluid. Reynolds numbers are varied from 2109 to 20,175 for transition and turbulent flow regimes. Heat transfer was enhanced over the whole tube length. The enhancement ratios were from 1.21 to 1.84. The largest enhancement ratio occurred in the transition flow regime. The heat transfer enhancement mechanism are due to the multiscale heat transfer tube, the modulated flow field with larger velocity and velocity gradient near the wall, and the enhanced flow turbulence intensity.

Here we created a new method using microflows through mesh pores to mitigate flow field. Consecutive conical-mesh inserts were suspending in a long tube, dividing the tube cross section into a near wall region and a bulk flow region. The central idea had the following aspects: (1) *Flow field modulation*: Microflows through mesh pores with suitable throttle effect decrease flow rate over the bulk flow region. Velocities and velocity gradients are significantly large near the tube wall. The method generated a totally inverse velocity distribution to that in a bare tube. (2) *Pressure*

balance effect: Mesh pores within the porous membrane balance pressures between upstream and down of mesh inserts. This avoids curious flow field distribution and ensures quasi-uniform hydraulic boundary layer on the tube wall. (3) *Decrease of pressure drop rise penalty*: The inclined mesh screen surface weakens the pressure rise effect while enhancing heat transfer. The configuration is much better compared with that when a flow jet impacts a perpendicular mesh screen surface.

We note that conical-mesh inserts can be made from stainless steel or copper mesh screen pieces, which are commercialized and cheap. MHTT has potential engineering applications. The paper was organized as follows. Section 2 described MHTT structure and 3D to 2D conversion of mesh pores. Section 3 described numerical simulation details. Section 4 (results and discussion) is a key section, including four subsections. Section 4.1 validated our numerical simulations. Section 4.2 described thermal–hydraulic behavior of MHTT. Section 4.3 summarized new numerical findings. Section 4.4 explained observed phenomena, focusing on heat transfer enhancement mechanism and decreased pressure drop rise penalty. Effects of various parameters on MHTT were also explained.

2. The modulated heat transfer tube (MHTT)

2.1. The MHTT structure

The conical-mesh insert was made of mesh screen with suitable *PPI* (pores per inch). Different from the mesh cylinder inserts [14–17], the inclined mesh pore membrane further reduces pressure drops while enhancing heat transfer. Fig. 1(a) shows the modulated heat transfer tube (MHTT) with conical-mesh inserts. A two-dimensional coordinate system was established, with r as the radial coordinate and x as the axial flow coordinate. The tube inside diameter was D. The first conical-mesh insert started from the tube entrance of L_1. The diverging angle of the conical-mesh insert was α. The diameter at the exit plane was δ. A periodic unit of the tube having one conical-mesh insert had a length of S. The total tube length was $L_1 + L_2$, where L_2 was the length that was populated by consecutive conical-mesh inserts. The following parameters are involved in this study: $D = 20.0$ mm, $L_1 = 100.0$ mm, $L_2 = 500.0$ mm, $\delta/D = 0.6$, 0.7 and 0.8, $S/D = 2$, 2.5 and 3, $PPI = 80$, 200 and 400, $\alpha = 60°$.
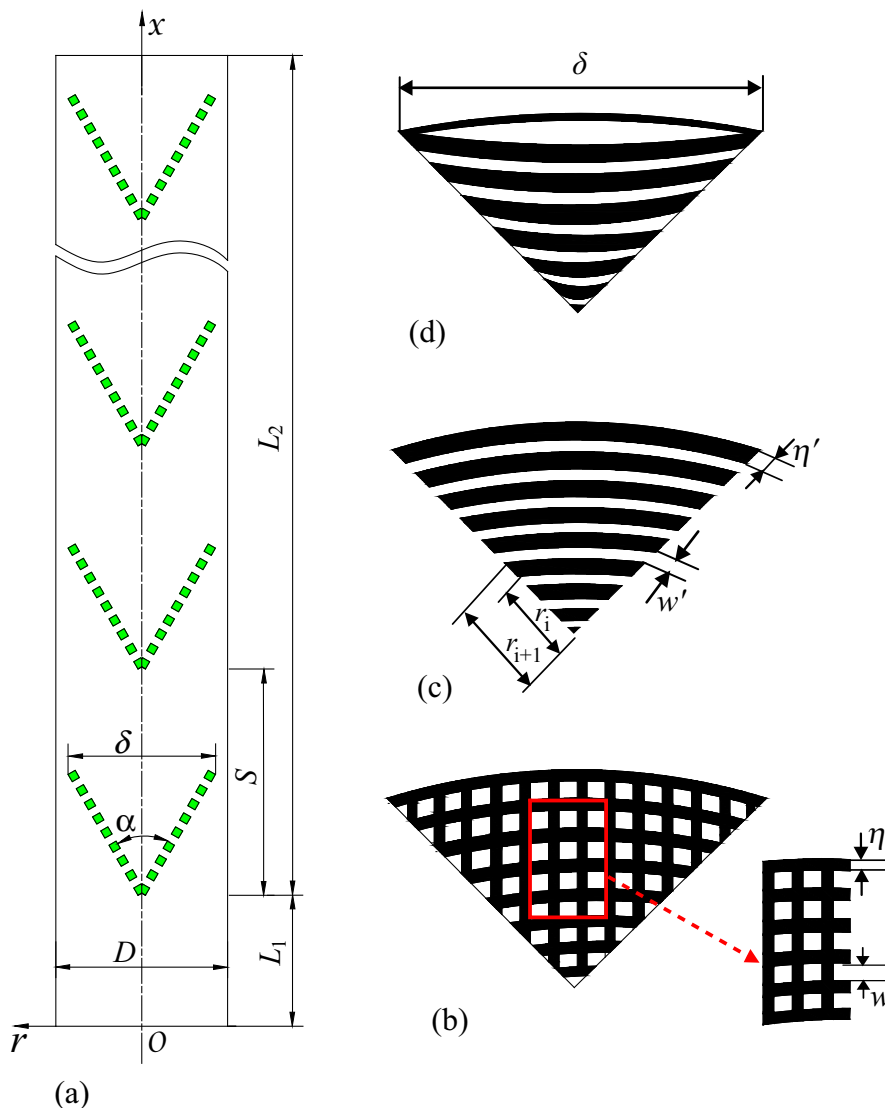
Fig. 1. The proposed MHTT and 3D to 2D conversion of the mesh screen.

2.2. The 3D to 2D conversion of mesh pores

MHTT is a three-level multiscale system: (1) micron scale of the mesh pore size; (2) miniature scale between tube wall and tip of the conical-mesh insert; (3) meter scale of the tube length. The multiscale computation was complex and needed large computation resource. For example, there are 31,915 mesh pores with $D = 20.0$ mm, $L_2 = 500.0$ mm, $PPI = 400$, $\alpha = 60°$, $\delta = 16.0$ mm and $S = 40.0$ mm. For each mesh pore, the three-dimensional simulation is necessary. The microflow of such huge number of mesh pores in micron scale is difficult to be simulated. We provided the 3D to 2D conversion of mesh pores to simplify the problem. Fig. 1(b) shows a fan-shaped mesh screen piece to be fabricated as a conical-mesh insert. The mesh pore had a clear width of w and the mesh wire had a thickness of η. The three-dimensional mesh screen (see Fig. 1(b)) can be converted to a two-dimensional one (see Fig. 1(c)), with an equivalent mesh pore width of w' and a mesh wire width of η'. The following criteria should be satisfied for such conversion.

2.2.1. The equivalent mesh pore width criterion

The square mesh pore had the equivalent diameter of $D_e = 4w^2/(4w) = w$ (see Fig. 1(b)). Meanwhile, the stripe-type mesh pores (see Fig. 1(c)) had the equivalent diameter as:

$$D'_e = 4 \times \frac{0.5(\alpha r_{i+1}^2 - \alpha r_i^2)}{\alpha r_{i+1} + \alpha r_i} = 2w' \tag{1}$$

where r_i and r_{i+1} are the radial length for i^{th} and $(i+1)^{th}$ stripe mesh wires, respectively. Based on the equal equivalent diameter criterion, $w' = 0.5w$.

2.2.2. The mesh pore area criterion

For the 3D mesh screen (see Fig. 1(b)), the total flow area of mesh pores is

$$A = \frac{0.5\alpha \times r^2}{(w + \eta)^2} \times w^2 \tag{2}$$

For the 2D mesh screen, the total flow area was

$$A' = \sum_{i=1}^{2r/(w'+\eta')} 0.5 \times \alpha \times (r_{i+1}^2 - r_i^2) = 0.5\alpha \times w' \times r \times \frac{r}{w' + \eta'} \tag{3}$$

The equal total flow area of mesh pores yields $\eta' = \eta + \eta^2/2w$. Table 1 lists the 3D to 2D conversion results for three PPI values of 80, 200 and 400, in which w, η, w' and η' are included.

Conversion of 3D to 2D mesh screen yields the stripe-type mesh screen (see Fig. 1(c)). Winding the stripe-type mesh screen forms the conical-mesh (see Fig. 1(d)). Periodic arrangement of various stripe-type conical-mesh inserts in the tube forms MHTT shown in Fig. 1(a).

3. The numerical simulation

3.1. Governing equations and boundary conditions

We focused on the effects of PPI, δ and S on the laminar heat transfer, in which $PPI = 80, 200, 400$, $\delta/D = 0.6, 0.7, 0.8$, $S/D = 2.0$, 2.5 and 3.0. Water was used as the working fluid. The Reynolds

numbers were in the range of 100–1500. The following assumptions were made:

- Steady flow and heat transfer.
- Rigid mesh screen without vibration during the flow and heat transfer processes.
- Incompressible fluid and constant physical properties of the fluid.
- Zero tube wall thickness thus the constant heat flux boundary condition was applied.

The two-dimensional flow and heat transfer in the tube including the stripe-type mesh pores had the following governing equations:

$$\nabla \cdot (\rho \vec{v}) = 0 \tag{4}$$

$$\nabla \cdot (\rho \vec{v} \vec{v}) = -\nabla p + \nabla \cdot [\mu(\nabla \vec{v} + \nabla \vec{v}^{\mathrm{T}})] + \rho \vec{g} \tag{5}$$

$$\nabla \cdot (\rho C_p T \vec{v}) = \nabla \cdot (\lambda \nabla T) \tag{6}$$

Fig. 2(a) shows the half computation domain due to the symmetrical behavior of the tube. A unit of the tube section including a conical-mesh insert was shown in Fig. 2(b). An attached coordinate system was fixed on the periodic unit, with o' as the starting point, x' as the attached axial coordinate, r as the radial coordinate. The tube entrance at $x = 0$ had the following velocity distribution:

$$u_{in} = 2u_{ave}\left[1 - \left(\frac{2r}{D}\right)^2\right] \tag{7}$$

where u_{ave} is the inlet average velocity. The Reynolds number characterizing the flow and heat transfer was defined as

$$Re = \frac{\rho D u_{ave}}{\mu} \tag{8}$$

where ρ and μ are the fluid density and viscosity, respectively. Once Re is given, u_{ave} was specified. The fluid had a constant temperature T_{in} at $x = 0$. The boundary conditions (BC) were summarized as follows:

Inlet BC at $x = 0$: $u = u_{in}$ given by Eqs. (7) and (8), $v = 0$, $T = T_{in}$.
Outlet BC at $x = L_1 + L_2$: $p = 1.013 \times 10^5$ Pa.
Wall BC at $r = 0.5D$: $u = v = 0$, $q = q_w$.
Symmetrical BC at $r = 0$: $v = 0$, $\frac{\partial u}{\partial r} = \frac{\partial T}{\partial r} = 0$.

Due to the periodic feature of the conical-mesh inserts, periodic boundary conditions (BC) exist and they are

$$u(x, r) = u(x + S, r) \tag{9}$$

$$v(x, r) = v(x + S, r) \tag{10}$$

$$p(x, r) = -\beta x + \tilde{p}(x, r) \tag{11}$$

$$\beta = \frac{p(x, r) - p(x + S, r)}{S} = \frac{p(x + S, r) - p(x + 2S, r)}{S} \tag{12}$$

$$\tilde{p}(x, r) = \tilde{p}(x + S, r) \tag{13}$$

$$T(x, r) = \theta x + \tilde{T}(x, r) \tag{14}$$

$$\theta = \frac{T(x + S, r) - T(x, r)}{S} = \frac{T(x + 2S, r) - T(x + S, r)}{S} = \frac{Q}{m C_p S}$$
$$= \frac{4q_w}{D \rho C_p u_{ave}} \tag{15}$$

$$\tilde{T}(x, r) = \tilde{T}(x + S, r) \tag{16}$$

Table 1
The 3D to 2D conversion of the used mesh screen parameters.

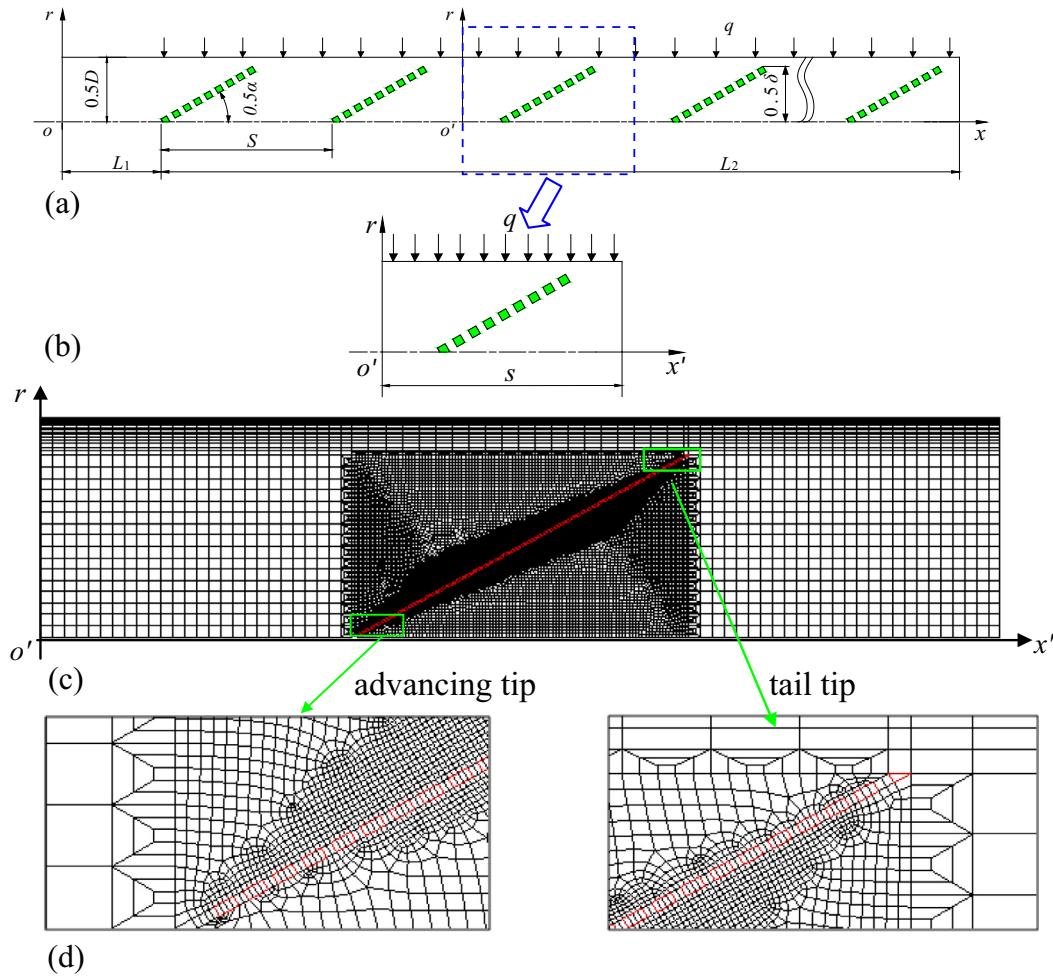| PPI	w	η	w'	η'
80	194	130	87	173
200	76	47	38	62
400	38	25	19	33

Fig. 2. The computation domain and grid generation: (a) full length computation domain, (b) computation domain for a periodic unit, (c) grid generation, (d) locally enlarged grid generation at the advancing tip and tail of the conical mesh insert.

Eqs. (9)–(16) were written by citing Refs. [18–20]. It is noted that the periodic unit of the conical-mesh insert starts and ends at the center of two neighboring conical-mesh inserts. Flow field should be carefully simulated near mesh pores. This is because flow through the mesh holes apparently influences the bulk flow field to determine the heat transfer. However, due to very thin mesh wire thickness typically in micron scale, thermal conduction was only considered in the space excluding the mesh wire thickness. In other words, thermal conduction was neglected within the mesh wires. The thermal insulation BC was applied at the mesh wire surface as

$$\left.\frac{\partial T}{\partial n}\right|_{\text{mesh surface}} = 0 \tag{17}$$

3.2. Grid generation and solution strategy

This study used the multiscale grid generation technique, which was similar to that in Refs. [14,16,17]. The periodic boundary condition required the same BC on the two periodic planes, which were linked together in GAMBIT 2.2.3. The divided block grid generation method was applied to improve the grid quality. Triangle block grids were created near mesh pores but rectangle block grids were created in regions far away from the mesh screen (see Fig. 2(c)). The PPI values are from 80 to 400. Fig. 2(c) and (d) shows grid generations for PPI = 80, having following features.

In the region with rectangle block grids, a uniform grid size of 500 μm was applied along the flow direction except near mesh pores. In the region with rectangular block grids, non-uniform grids were used in radial direction. The bulk region used 500 μm grid size, but the first fluid layer near the tube wall had 25 μm size, respectively. The grids were gradually refined from the bulk region to the near wall region.

In the near mesh pore region, triangle block grids were used. The quad-pave grid generation method was applied near and within the mesh pores. Grids gradually became coarse far away from the mesh pores. Fig. 2(d) shows the generated grids at the advancing tip and tail tip of the conical-mesh insert. Three levels of grids can be seen. The finest grids of 43.5 μm × 43.5 μm were used near and within mesh pores. The second level of grids had the size of 100 μm × 100 μm away from the mesh pores. The normal grids of 500 μm × 500 μm were used in the bulk flow region. The three levels of grids were linked together by the adapting factor of 5:1 regarding the grid bridging.

It is noted that the above description was for the PPI = 80 mesh insert tube. More fine grids were used for PPI = 200 and 400 mesh insert tubes. Sensitivity analysis was performed when different grid size and number were used. Especially, grid sizes near and within mesh pores were carefully selected so that the final results were independent on more refined grid sizes.

The FLUENT software (6.3.26 version) solved Eqs. (5)–(7) subject to boundary conditions. The Gambit 2.2.3 module created the grid generation and computation domain. The finite volume

method discretized the governing equations. The second order upwind scheme was applied for the momentum and energy conservation equations. For the multiscale grids linking, several high-skewness grids existed. The SIMPLEC algorithm amended the grid skewness, treating the coupling of pressures and velocities. The under-relaxation factors were 0.2 for pressures and 0.5 for momentum equations, ensuring the convergence and stability of the numerical simulation. Because grids were very fine near and within mesh pores, the residual error was 10^{-16}, several orders smaller than that used in the literature. The computation was converged if the residual error for tracking parameters was smaller than 10^{-16} and the velocities at specific locations did not change anymore. The simulations were run on a Dell work station, that had two 8-core CPUs (2.4 GHz each) and 24 GB of RAM. The computation needs about 0.5 h for each run. Table 2 shows all the runs studied in this paper, BT means bare tube without insert, q was fixed so that the fluid temperature difference between the tube outlet and inlet was 10 °C for each run. Thus, the constant physical property assumption is valid. Several cases were included in each run, with PPI = 80, 200 and 400, S/D = 2.0, 2.5 and 3.0, δ/D = 0.6, 0.7 and 0.8.

3.3. Data reduction

The flow and temperature fields were obtained after convergence of the numerical simulation. The non-slip BC on the wall ($u_w = 0$) was used. The first fluid layer on the tube wall had a 25 μm thickness. The wall heat flux was conducted through the fluid layer. The fluid temperature within this layer was T_{grid}. The Fourier thermal conduction law yields

$$q = -\lambda \frac{\partial T}{\partial r}\bigg|_{r=0.5D} \tag{18}$$

Thus, the wall temperature T_w was computed as

$$T_w = \frac{qy}{\lambda} + T_{grid} \tag{19}$$

where $y = 2.5 \times 10^{-7}$ m. The local Nusselt number was

$$Nu_x = \frac{q}{T_w - T_f} \times \frac{D}{\lambda} \tag{20}$$

where T_f is the fluid temperature over the whole tube cross section, which was

$$T_f = \frac{\int \rho C_p u T dA}{\int \rho C_p u dA} \tag{21}$$

Table 2
Runs computed for BT and MHTT.

Runs	Tubes	m (kg/s)	u_{ave} (m/s)	Re	q (w/m²)
1	BT	0.00113	0.0036	100	1503.18
2	MHTT	0.00113	0.0036	100	1503.18
3	BT	0.00339	0.0109	300	4509.53
4	MHTT	0.00339	0.0109	300	4509.53
5	BT	0.00565	0.0181	500	7515.89
6	MHTT	0.00565	0.0181	500	7515.89
7	BT	0.00791	0.0253	700	10522.25
8	MHTT	0.00791	0.0253	700	10522.25
9	BT	0.01017	0.0326	900	13528.60
10	MHTT	0.01017	0.0326	900	13528.60
11	BT	0.01243	0.0398	1100	16534.96
12	MHTT	0.01243	0.0398	1100	16534.96
13	BT	0.01469	0.0470	1300	19541.31
14	MHTT	0.01469	0.0470	1300	19541.31
15	BT	0.01695	0.0543	1500	22547.67
16	MHTT	0.01695	0.0543	1500	22547.67

The overall Nusselt number was

$$Nu = \frac{q}{T_{w,ave} - T_{f,ave}} \times \frac{D}{\lambda} \tag{22}$$

where $T_{f,ave} = 0.5(T_{in} + T_{out})$ is the average fluid temperature and T_{in}, T_{out} are the inlet and outlet average fluid temperature, $T_{w,ave}$ is the average wall temperature, which is

$$T_{w,ave} = \frac{\sum_{i=1}^{n'} T_w}{n'} \tag{23}$$

where n' is the number of grids on the wall.

The Darcy friction factor is defined as

$$f = \frac{(\Delta p/S) \times D}{\rho u_{ave}^2/2} \tag{24}$$

where Δp is the pressure drop in a periodic unit, S is the periodic unit length. PEC (performance evaluation criterion) evaluates the comprehensive performance of MHTT, which is written as [21,22]

$$PEC = \frac{Nu/Nu_b}{(f/f_b)^{1/6}} \tag{25}$$

where Nu, f are for the MHTT and Nu_b, f_b are for the bare tube without inserts.

The heat transfer enhancement factor (EF) is defined as

$$EF = Nu/Nu_b \tag{26}$$

4. Results and discussion

4.1. Validation of the numerical simulations

This section verified how long beyond which the heat transfer can be fully developed, thus the periodic BC can be used. This section also compared our numerical results with analytical and numerical results reported in the literature.

Fig. 3(a) shows local Nu along x and x/D with Re = 300, PPI = 80, S/D = 2, δ/D = 0.6. Results in Fig. 3(a) were obtained using the whole tube length, instead of the periodic BC. Heat transfer is difficult to be fully developed for low Re. Generally, Nu was sharply decreased near the tube entrance to indicate the developing heat transfer. The decrease of Nu was weakened with increases of x/D and the Nu numbers were periodically repeated beyond about eight periodic units of the conical-mesh inserts ($x/D > 15$), indicating that fully developed heat transfer can be reached even for Re = 300. Thus, the periodic BC can be used. Fig. 3(b) shows the flow field focusing on the 8th unit. The computation was performed over the whole tube length. Large velocity and velocity gradient were found near the tube wall. Ahead of the inclined mesh membrane insert is the weak positive flow along the flow direction. Downstream of the porous membrane is the weak circulating flow. Alternatively, Fig. 3(c) shows the flow field using the periodic boundary condition. It was found that the periodic boundary condition gives the exact same flow field as the whole tube length computation. Comparing Fig. 3(b) and Fig. 3(c) shows the fully developed flow profiles for the 8th unit. Larger Re than 300 yields easy happening of the fully developed heat transfer. This paper focused on the discussion of fully developed heat transfer.

Fig. 4(a) compared our numerical results with theoretical solution for laminar flow and heat transfer in a bare tube. For fully developed heat transfer, the analytical solution yields Nu_{th} = 4.36 which is independent of Re and f_{th} = 64/Re which is inversely proportional to Re. Fig. 4(a) shows excellent agreement between numerical and theoretical results, with difference less than 1%.

Fig. 4(b) compared our numerical results with those in Ref. [23]. Sripattanapipat and Promvonge [23] studied laminar periodic flow
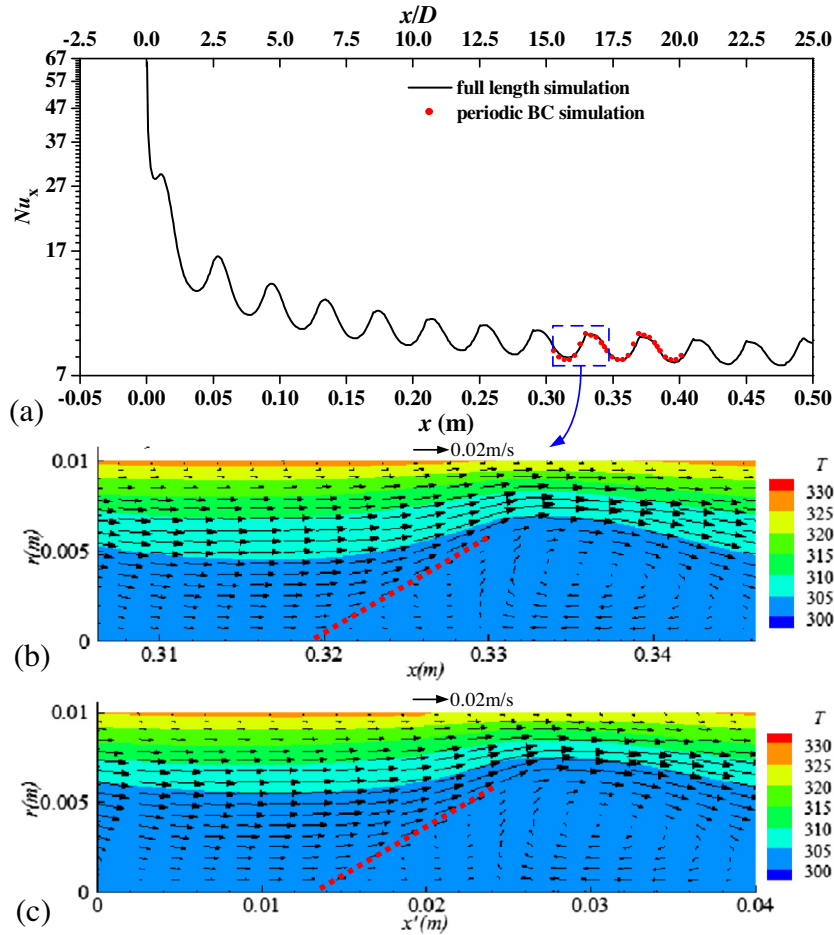
Fig. 3. The full length computation and periodic boundary condition computation for Nu_x versus x (PPI = 80, S/D = 2, δ/D = 0.6, Re = 300).
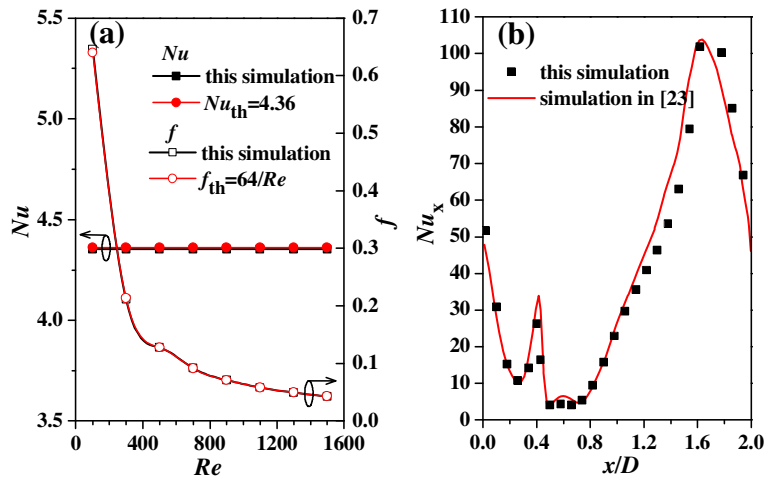

Fig. 4. Validation of the present numerical simulations: (a) comparison with the theoretical solution for bare tube, (b) comparison with Ref. [23] for baffle plate insert in tube.

and heat transfer in a two dimensional horizontal channel with isothermal walls and with staggered diamond-shaped baffles. The computations were based on the finite volume method, and the SIMPLE algorithm was implemented. The fluid flow and heat transfer characteristics were presented for Reynolds numbers (100–600) based on the channel hydraulic diameter. Effects of different baffle tip angles on heat transfer and pressure loss were studied

and the results of the diamond baffle were compared with those of the flat baffle. Fig. 4(b) shows our computation result compared with that in Ref. [23]. The running case was from Fig. 5 in Ref. [23] for flat baffle (baffle angle of 0°). D in Fig. 4(b) referred to the horizontal channel height. Our numerical results excellently matched that of Ref. [23], providing the evidence that our simulation is correct.

4.2. The thermal–hydraulic behavior for MHTT

We fixed the diverging angle as $\alpha = 60°$. The Reynolds number (Re), diverging diameter (δ), periodic unit length (S) and PPI of mesh screen influence heat transfer.
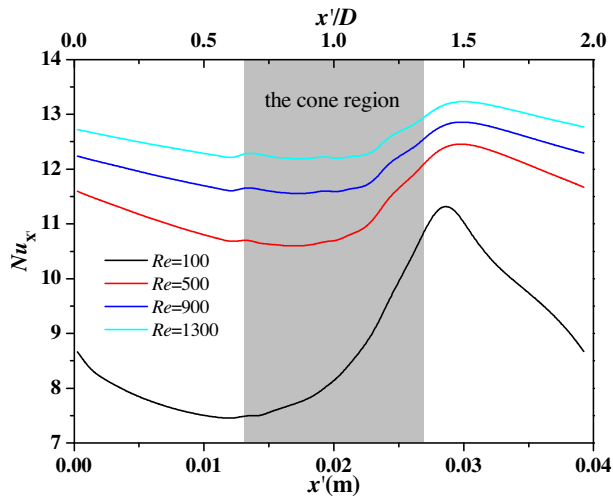
Fig. 5. Local Nu distribution along x'/D with PPI = 80, δ/D = 0.8 and S/D = 2.

4.2.1. Cases for PPI=80

The 80 PPI mesh screen yields the coarsest pore width of $w = 194$ μm (see Table 1). Fig. 5 shows the local Nu values against x' and x'/D for periodic developed flow. Four Re were selected as 100, 500, 900 and 1300. For each Re, the maximum Nu happened at the mesh cone downstream. The minimum Nu appeared within the mesh cone region, but the axial location is dependent on the Re. For low Re such as 100, the minimum Nu appeared at the beginning of the mesh cone. The increase of Re shifted the location downward. Nu was quite non-uniform for low Re. But quasi-uniform Nu along x'/D was observed for large Re such as 1300.

Fig. 6 shows bulk Nusselt Numbers (Nu) and friction factors (f) versus bulk Reynolds number (Re). The parameters of δ and S are combined to form two dimensionless parameters of δ/D and S/D. MHTT had Nu significantly larger than 4.36 for the bare tube, indicating significant heat transfer enhancement. Slopes of Nu versus Re were changed while raising Re. Large slopes were found for low Re such as Re < 500–700. Slopes of Nu with Re were decreased beyond Re = 500–700. Nu was increased with decreases in S/D (see Fig. 6(a)–(c)). Smaller S/D infers densely populated conical-mesh inserts along flow direction. The value of $S/D = 2$ is recommended here. We note that $D–\delta$ equals to two times of the annular gap width (see Fig. 6(a)). Large δ narrowed the annular gap width. Nu was increased by raising δ/D (see Fig. 6(d)). The annular gap width was 2.0 mm when $D = 20.0$ mm and $\delta/D = 0.8$. The bulk Nu covered
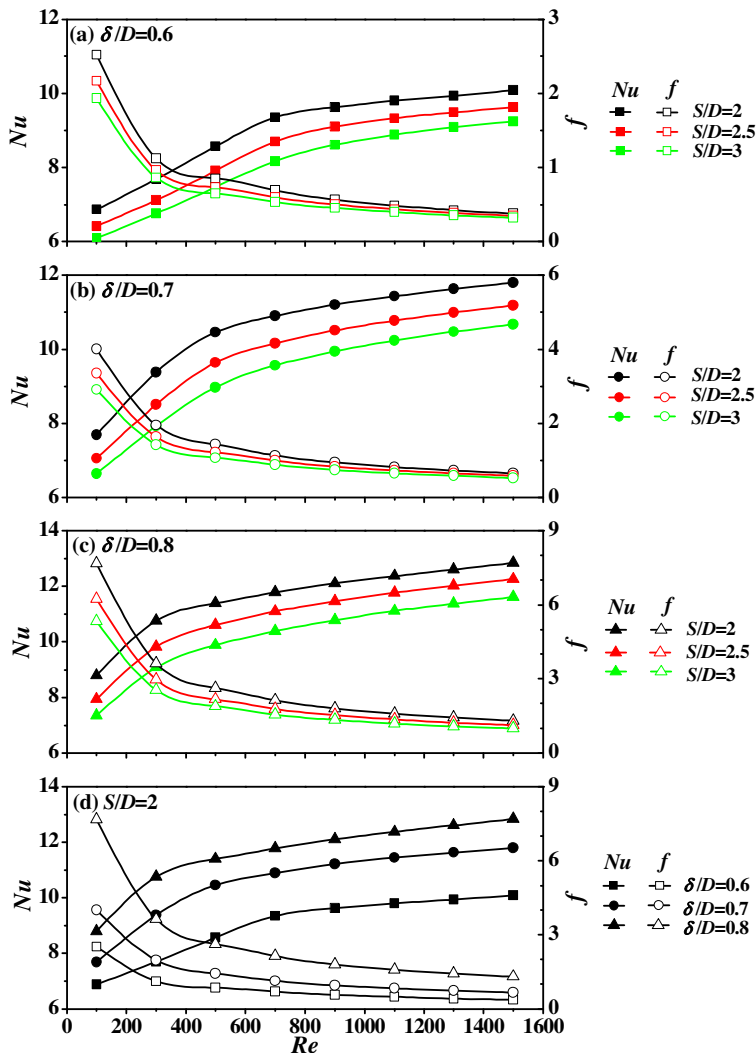
Fig. 6. The Nusselt number and fraction factor for PPI = 80 (w = 194 μm, η = 130 μm).
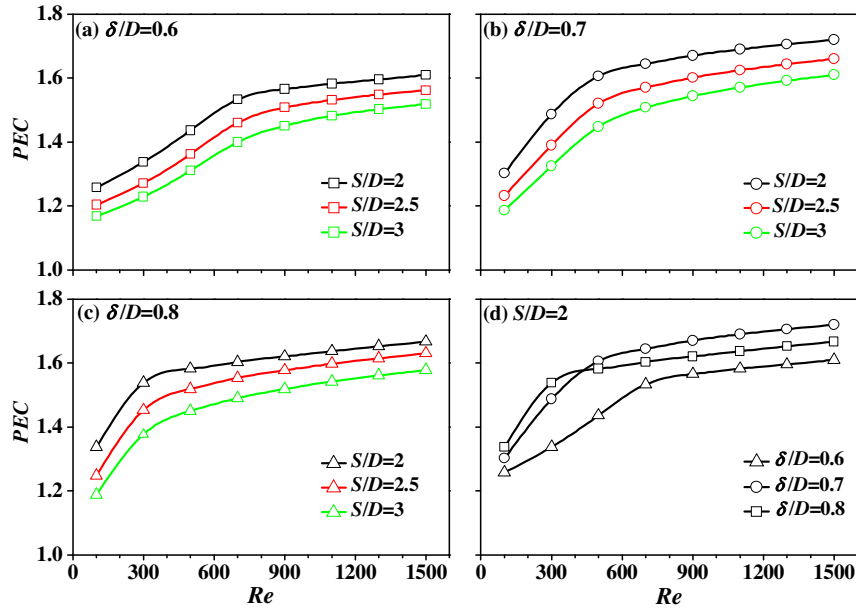
Fig. 7. *PEC* versus *Re* for *PPI* = 80 (*w* = 194 μm, *η* = 130 μm).
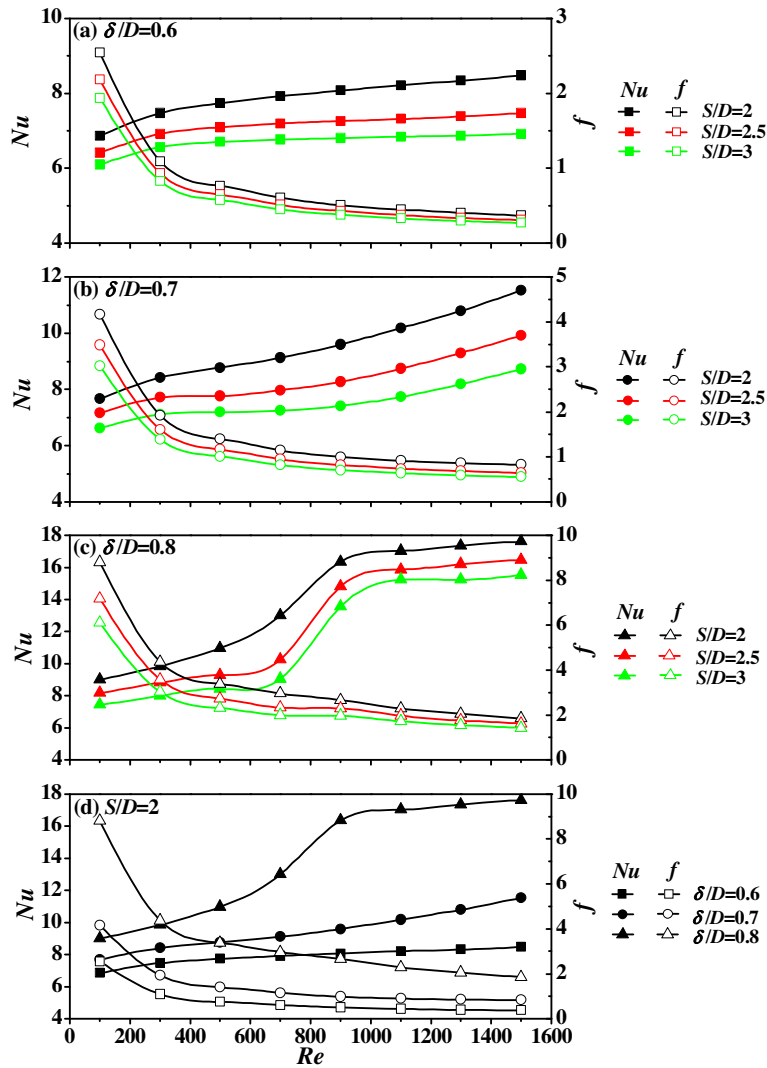
Fig. 8. Nusselt number and fraction factor for *PPI* = 400 (*w* = 38 μm, *η* = 25 μm).

the range of 6.1–12.8 (see Fig. 6), which was 1.4–2.9 times of that for bare tube.

The friction factor (f) represents the pressure drop variations with Re. It was found that f was decreased with increases in Re. For each subfigure in Fig. 6, f was decreased sharply at low Re. But slopes of f against Re become gentle beyond the transition Reynolds number in a narrow range of 400–500. The PEC value evaluates how much of the pressure drop rise for a specific heat transfer enhancement. Usually, a heat transfer device can be used for PEC larger than one. The larger the PEC, the better the heat transfer device is. Fig. 7 shows PEC for PPI = 80. The change trends of PEC versus Re, S/D and δ/D are similar to those of Nu. PECs are increased with increases in Re. They can be elevated by increasing

δ/D and/or decreasing S/D. An exception was found in Fig. 7(d), in which PEC curves are intercrossed for $\delta/D = 0.7$ and 0.8. For $Re < 430$, PECs with $\delta/D = 0.8$ are slightly larger than those with $\delta/D = 0.7$. But $\delta/D = 0.7$ cases held larger PECs than $\delta/D = 0.8$ beyond the crossing point at $Re = 430$.

4.2.2. Cases for PPI=400

The cases of PPI = 400 yields finest mesh pore size with pore width of $w = 38$ μm and wire thickness of $\eta = 25$ μm. The 3D to 2D conversion reaches $w' = 19$ μm and $\eta' = 33$ μm. The change trends of Nu and f versus Re, S/D and δ/D are similar to those for PPI = 80. The difference lied in the higher Nusselt numbers for PPI = 400 than those for PPI = 80 (see Figs. 8 and 6). The optimal
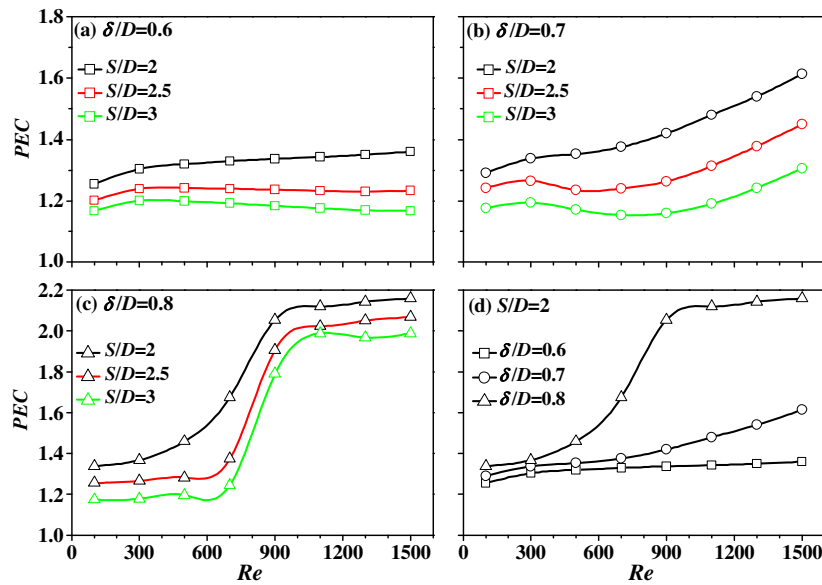
Fig. 9. PEC versus Re for PPI = 400 ($w = 38$ μm, $\eta = 25$ μm).
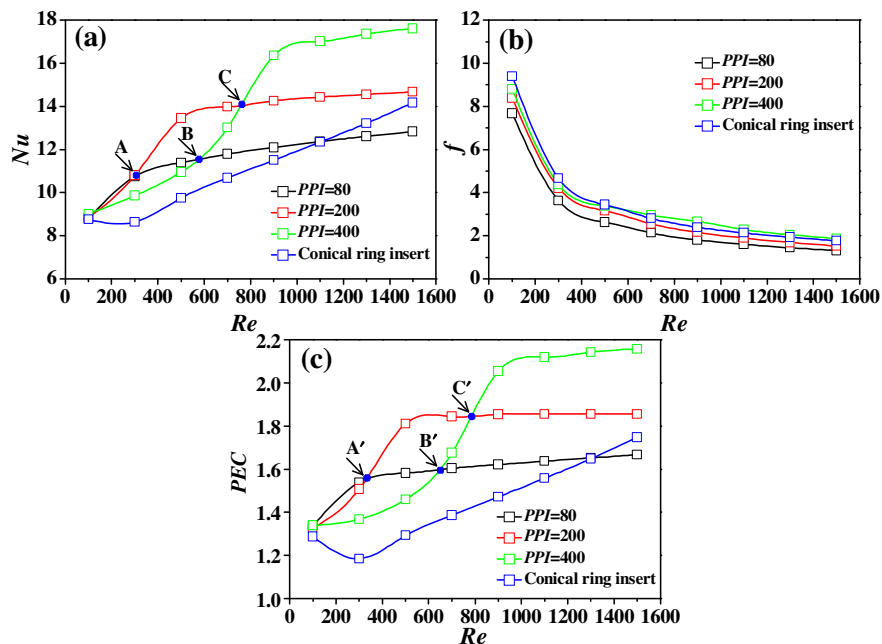
Fig. 10. Effect of PPI on Nu, f and PEC with $S/D = 2$ and $\delta/D = 0.8$.

δ/D and S/D are 0.8 and 2.0, respectively. There are three types of change trends of PEC versus Re (see Fig. 9). The first type regards PEC almost independent of Re for $\delta/D = 0.6$ (large annular gap width, see Fig. 9(a)). The second type involves the increased PECs while increasing Re for $\delta/D = 0.7$ (moderate annular gap width, see Fig. 9(b)). The third type regards a narrow Re transition regime across which PECs are switched from a lower platform value to a higher platform value for $\delta/D = 0.8$ (sees Fig. 9(c)). The Re transition range was Re = 700–1000. The two PEC platform values were 1.26 before the transition and 2.0 after the transition with $\delta/D = 0.8$ and $S/D = 2.5$. The three curves in Fig. 9(d) also represented the three types of change trends of PECs versus Re. One should remember in mind that the PPI = 400 mesh inserts generate PEC up to 2.2, maximally.

4.3. Numerical findings on MHTT

The tube with conical ring insert without holes was studied previously [11,24,25]. For comparison purpose, results for such configuration were plotted in Fig. 10. Regarding MHTT, three key points

were paid attention: (1) significant heat transfer enhancement of MHTT; (2) varied slopes of Nu versus Re; and (3) intercrossed Nu and PEC curves among different PPI conical mesh inserts.

MHTT had Nu = 8.8–17.6, which are 2.02–4.1 times of that for a bare tube ($Nu_{th} = 4.36$ for fully developed heat transfer). Such high heat transfer enhancement ratios are difficult to be achieved by other techniques. The conical ring inserts without holes also enhanced heat transfer, but Nu was significantly lower and f was larger than those for MHTT (see Fig. 10(a) and (b)).

Nu was increased while raising Re, but slopes of Nu versus Re were decreased with increases of Re (see Fig. 10). There is a transition Re, beyond which Nu and PEC are only slightly increased. In other words, high platform Nu and PEC values can be approached. The transition Re depends on PPI. High PPI conical-mesh inserts delayed the transition Re and elevated the platform Nu and PEC values. For PPI = 200, the transition Re was about 500 and the platform Nu was about 14.6. For PPI = 400, the transition Re was about 900 and the platform Nu was about 17.6. The transition Re and platform value phenomenon also existed for PEC (see Fig. 10(c)).
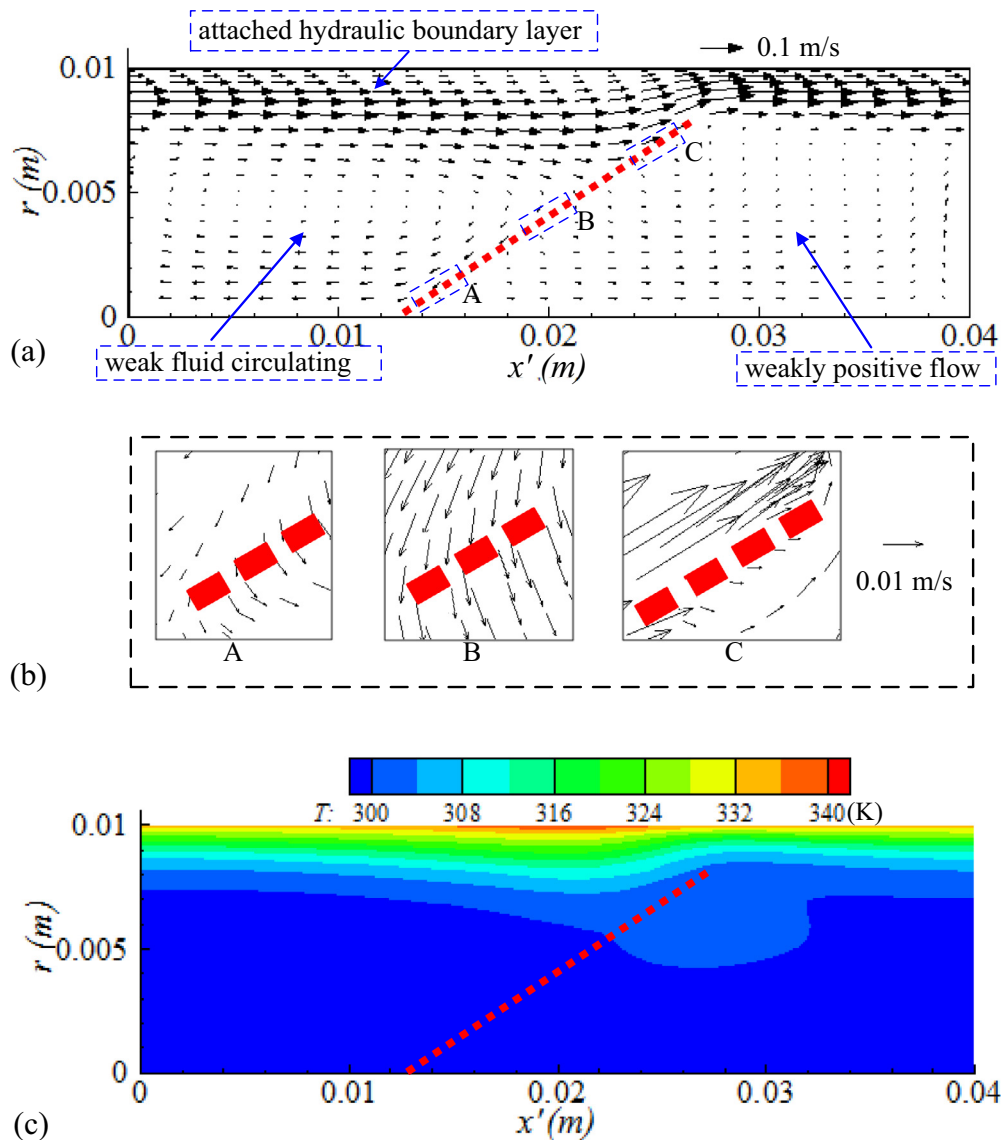
Fig. 11. The flow and temperature fields for PPI = 400 conical-mesh insert with Re = 900, $\delta/D = 0.8$ and $S/D = 2$.
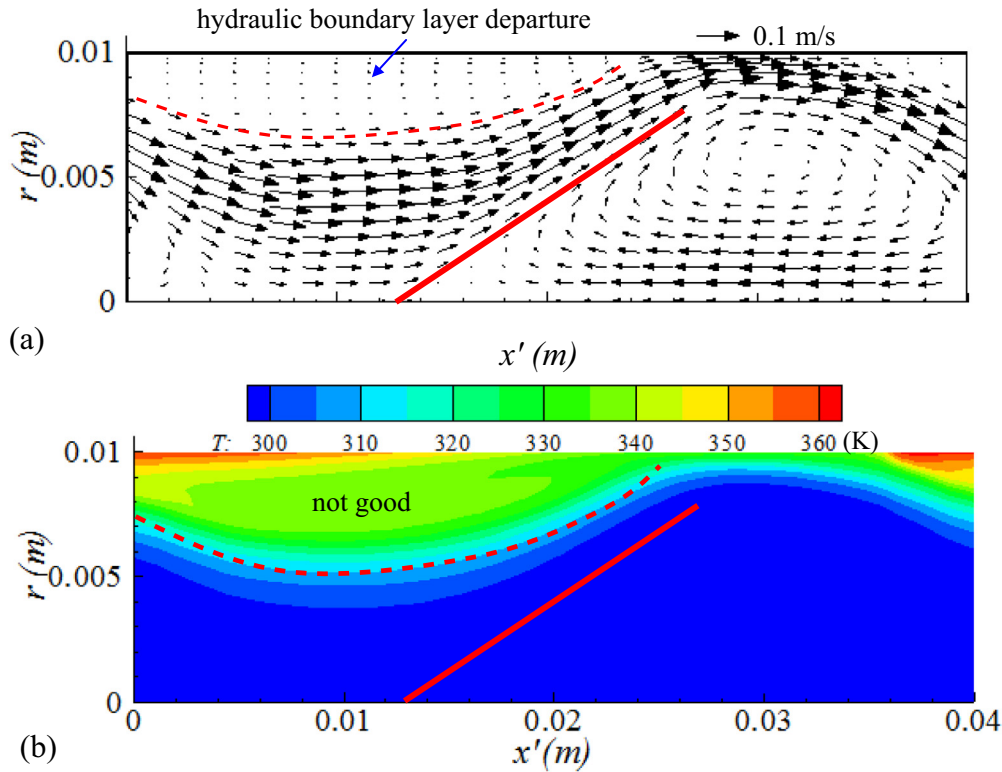
Fig. 12. The flow and temperature fields for conical-ring insert (no holes) with $Re = 900$, $\delta/D = 0.8$ and $S/D = 2$.
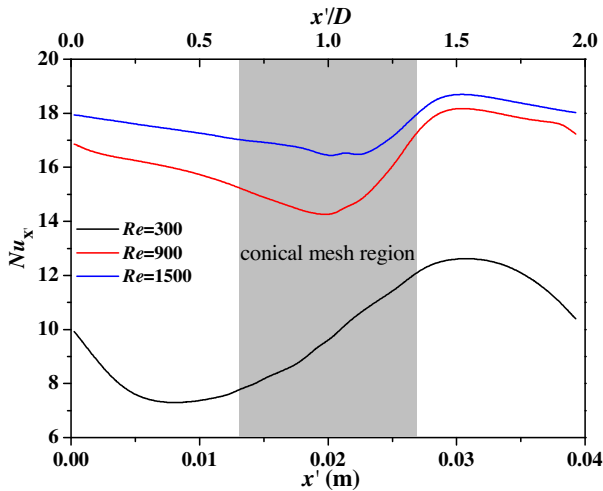
Fig. 13. Effect of Re on local Nu variations with $PPI = 400$, $\delta/D = 0.8$ and $S/D = 2$.

Nu and PEC curves are intercrossed among different PPI values. The crossing points were marked as A, B and C for Nu in Fig. 10(a) and A', B' and C' for PEC in Fig. 10(c). For example, Nu curves for $PPI = 200$ and 400 are crossed on C at which $Re = 800$, below which Nu and PEC are larger for $PPI = 200$, beyond which they are larger for $PPI = 400$. It is better to use low PPI mesh inserts at low Re, but use high PPI mesh inserts at large Re.

4.4. Explanation of observed phenomena

4.4.1. Heat transfer enhancement mechanisms

Based on the classical fluid mechanics theory, a bare tube without inserts has parabola axial velocity distribution over the tube
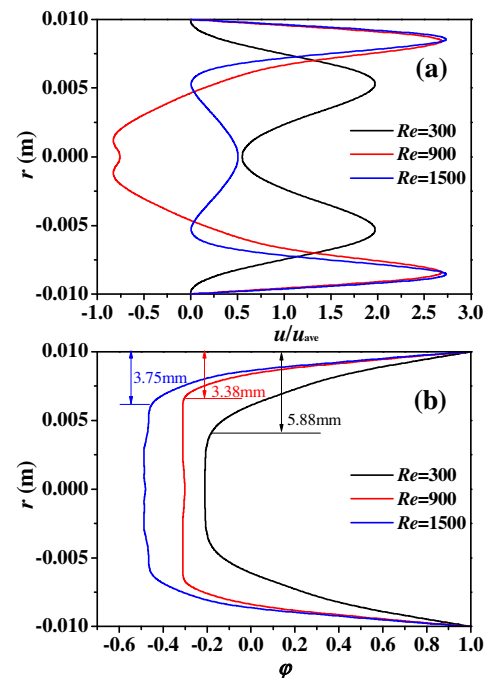
Fig. 14. Effect of Re on axial velocity and fluid temperature distributions over the tube cross section at $x' = 0.01$ m with $PPI = 400$, $\delta/D = 0.8$ and $S/D = 2$ ($\varphi = (T - T_{f,x'=0.01})/(T_w - T_{f,x'=0.01})$. (For interpretation of the references to color in this figure legend, the reader is referred to the web version of this article.)

cross section. The velocities near the tube wall are smaller than those in the bulk flow region to limit the heat transfer. Inserting a conical-mesh insert successfully modulated the flow field to improve the heat transfer (see Fig. 11(a)). Within the half

computation domain of a periodic unit, the flow field can be divided into three distinct regions. Region 1 is called the attached hydraulic boundary layer region, having quasi-parallel streamlines and ultra-large velocity and velocity gradient. Region 2 is called the weak fluid circulating region, located in the bulk flow region ahead of the conical-mesh insert. Region 3 is called the weakly positive flow region in the bulk flow region downstream of the conical-mesh insert. Region 2 plus region 3 constitute the bulk flow region. The three-region flow field is benefitted from the inclined mesh screen membrane. First, the throttle effect by micron-scale mesh pores weakens flow velocities in the bulk flow region, leaving large part of flow rate flowing near the tube wall. Second, mesh pores balance pressures across the mesh screen membrane to some degree, ensuring an attached hydraulic boundary layer near the tube wall. Third, the weakly positive flow region receives flow rates due to microflows through mesh pores.

Three local areas across the two sides of the inclined mesh insert were selected as *A*, *B* and *C*, which were located near the advancing tip, at the center of the mesh insert and at the tail tip of the mesh insert, respectively. Fig. 11(b) shows the local flow fields on these areas. We note the velocity scale of 0.1 m/s in Fig. 11(a) and 0.01 m/s in Fig. 11(b). It is seen that flow velocities in *A* and *B* area were about one order magnitude smaller than that in the attached hydraulic boundary layer, indicating the successful flow field modulation. Because the area *C* was close to the attached hydraulic boundary layer, the area *C* had relative larger velocity. The attached hydraulic boundary layer creates a quasi-uniform and thin thermal boundary layer (see Fig. 11(c)), accounting for the significant heat transfer enhancement mechanism.

On the contrary, a tube with conical-ring inserts without holes creates poorer flow and temperature fields (see Fig. 12(a) and (b)). There is no mass transport across the plate. Pressures cannot be balanced across the plate. The streamlines are severely deformed, yielding a hydraulic boundary layer departure region near the tube wall. Near the tube wall, large velocities only appeared downstream of the solid plate. Regarding the bulk flow region, large velocities appear ahead of the conical plate but strong vortex is observed downstream of the conical plate. Correspondingly, thermal boundary layers are not uniform and thick near the tube wall (see Fig. 12(b)). The deformed flow and temperature fields account for the poorer heat transfer performance than the conical mesh insert tube.

4.4.2. Varied slopes of Nu and PEC against Re

Slopes of *Nu* and *PEC* versus *Re* are changed while increasing *Re*. A transition *Re* exists, below which *Nu* and *PEC* are quickly increased but beyond which they are only slightly increased. Fig. 13 examined local *Nu* versus *x'* and *x'/D* in a periodic unit. All the parameters are the same except *Re* of 300, 900 and 1500. Nu'_x is significantly increased when *Re* is changed from 300 to 900, but the difference of Nu'_x is obviously weakened between *Re* = 900 and 1500.

We plotted the axial velocity and temperature distributions over the tube cross section at *x'* = 0.01 m, which is just ahead of the conical-mesh insert (see Fig.14). The axial velocities are scaled by u/u_{ave}, and the temperatures are scaled by $\varphi = (T - T_{f,x'=0.01})/(T_w - T_{f,x'=0.01})$. Examining u/u_{ave} and φ distributions identified the flow and temperature conditions near the tube wall. The velocity gradients in the attached hydraulic boundary layer are significantly larger for *Re* = 900 (red curve in Fig. 14(a)) than those for *Re* = 300 (black curve in Fig. 14(a)). But the increase of velocity gradients near the tube wall is weak when *Re* is increased from 900 to 1500. Local minimum velocities appeared at the tube centerline (*r* = 0) for *Re* = 300 and 900. But, local maximum velocity appeared at *r* = 0 for *Re* = 1500, slowing down fluid velocities near the tube

wall. Thermal boundary layers can be identified by examining temperature distributions in Fig. 14(b). The thermal boundary layers are apparently thinned from 5.88 mm to 3.38 mm when *Re* changed from 300 to 900. But the difference of thermal boundary layers is weak with *Re* from 900 to 1500. Figs. 13 and 14 explained the varied slopes of *Nu* versus *Re* while increasing *Re*.

4.4.3. Crossing curves of Nu among different PPI

We explained why crossing curves of *Nu* happen for different *PPI* mesh inserts. Fig. 15 shows Nu'_x versus *x'* and *x'/D* for *Re* = 500, 1100 and for *PPI* = 200, 400, respectively. At low *Re* of 500, the tube with *PPI* = 200 mesh insert had larger *Nu* than that with *PPI* = 400 mesh insert. On the contrary, at higher *Re* of 1100, the tube with *PPI* = 400 mesh insert had better performance. Nu'_x is quasi-uniformly distributed along *x'* except for that with *Re* = 500 and *PPI* = 400. Nu'_x is significantly deformed against *x'* for *Re* = 500 and *PPI* = 400.

Fig. 16 focused on the low *Re* case with *Re* = 500. The flow and temperature fields are compared between the tubes with *PPI* = 200 and 400 conical-mesh inserts. Fig. 16(a) shows a perfect flow region with *PPI* = 200 mesh insert: an attached hydraulic boundary layer having large velocity and velocity gradient, a weak fluid circulating region ahead of the mesh screen in the bulk flow region, and a weakly positive flow region downstream of the mesh screen in the bulk flow region. The flow field is similar to that shown in Fig. 11(a). Correspondingly, a quasi-uniform and thin thermal boundary layer was seen in Fig. 16(c).

Fig. 16(b) shows that when *PPI* equals to 400, the streamlines are deformed, deviating from the perfect flow field shown in Fig. 16(a). There was a hydraulic boundary layer departed from the tube wall, accounting for the poorer heat transfer performance. One remembers in mind that high *PPI* mesh screen had small mesh pore size, providing large throttle pressure drop for microflows through mesh pores. Flow field in a tube with ultra-high *PPI* mesh insert should approach that in a tube with plate insert without holes. Correspondingly, there was a "not good" region having high temperature and thick thermal boundary layer (see Fig. 16(d)).

Now we deal with the large *Re* cases with *Re* = 1100. The flow field for *PPI* = 200 is good but not optimized (see Fig. 17(a)). There was an attached hydraulic boundary layer to have large velocity and velocity gradient near the tube wall. But, because *PPI* = 200 is not optimized with the higher *Re* of 1100, the flow directions are positive in the whole bulk flow region. In other words, the weak circulating flow was not established upstream
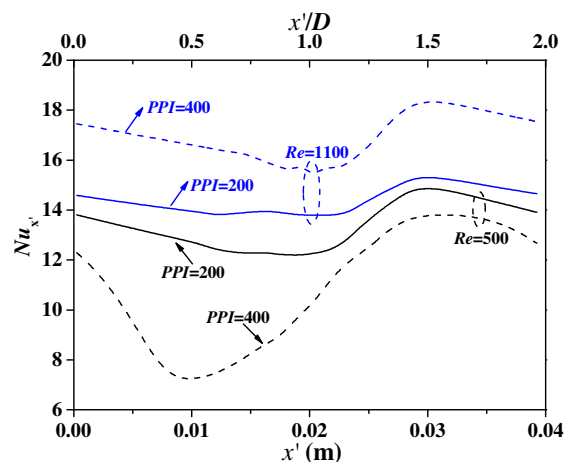

Fig. 15. Combined effects of *Re* and *PPI* on local *Nu* distributions with $\delta/D = 0.8$ and $S/D = 2$.
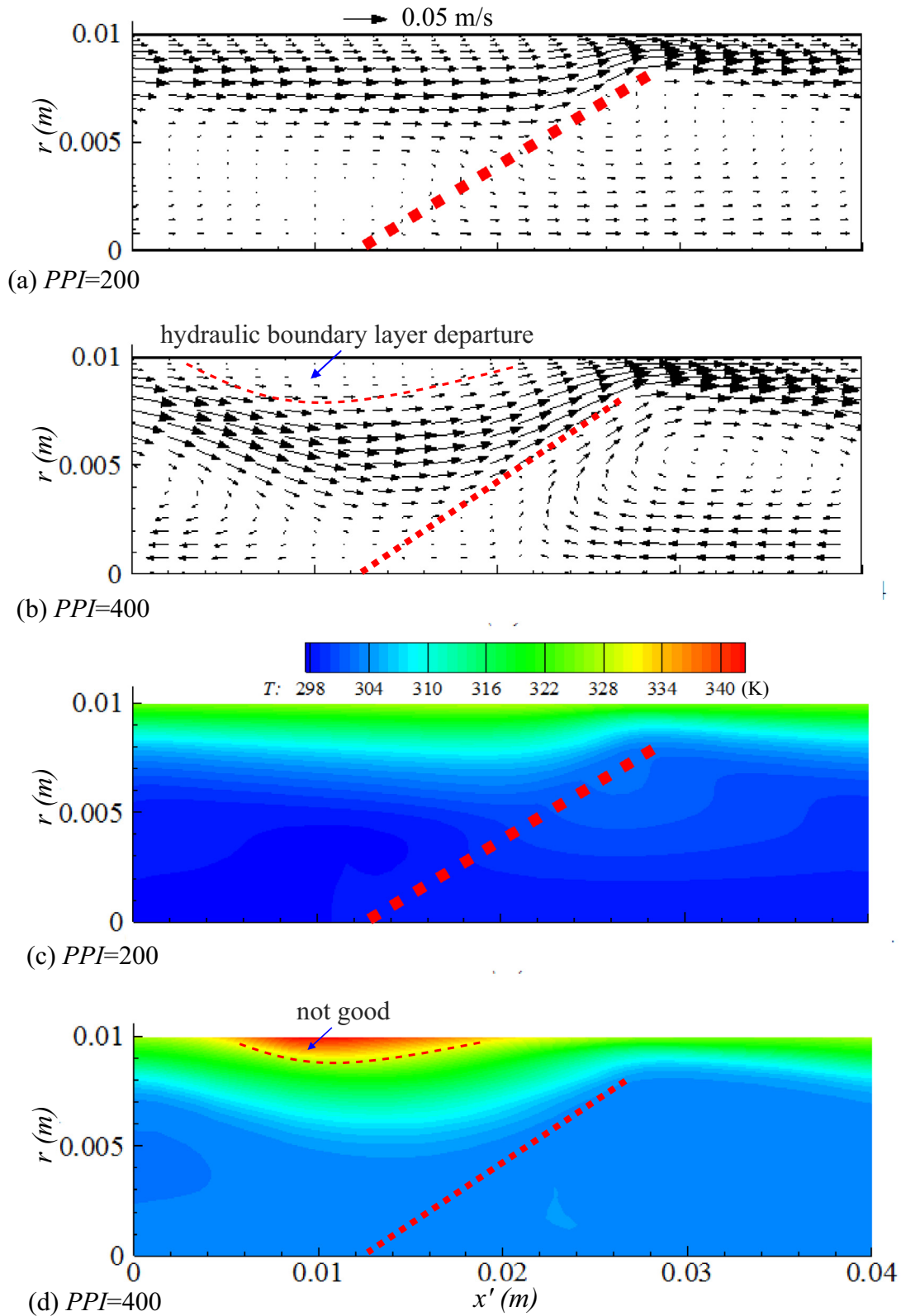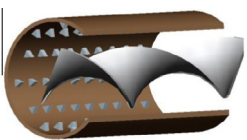
(a) PPI=200

(b) PPI=400

(c) PPI=200

(d) PPI=400

Fig. 16. Flow and temperature fields for PPI = 200 and 400 with Re = 500, δ/D = 0.8 and S/D = 2.

of the conical mesh screen, slowing down velocities near the tube wall. Fig. 17(c) shows the temperature field, correspondingly.

The situation is improved when PPI is increased, at which the mesh pore size is decreased to increase the throttle pressure drops

for microflows through mesh pores. Fig. 17(b) shows the perfect flow field with weak circulating flow established upstream of the conical mesh screen, further increasing velocity and velocity gradient near the tube wall.
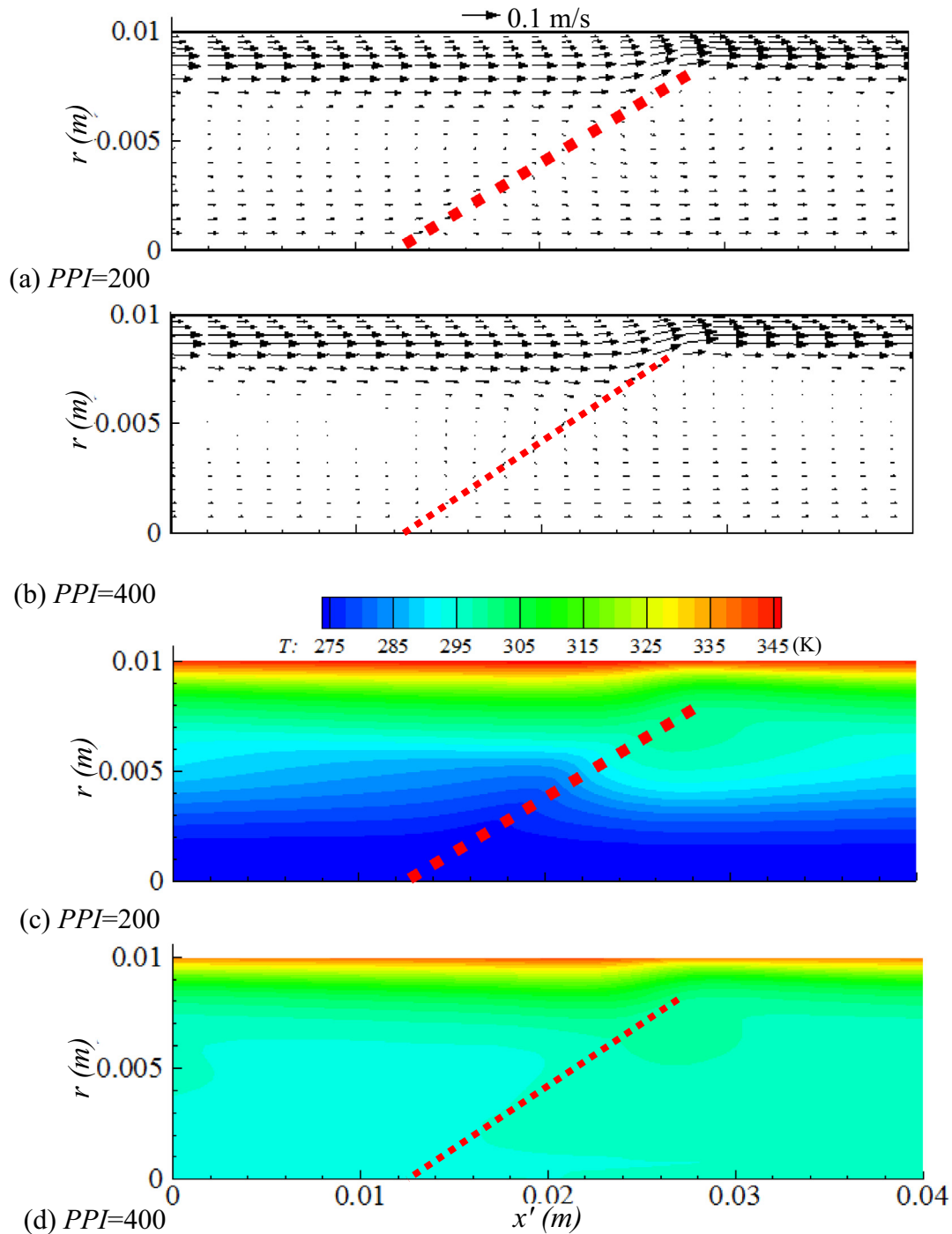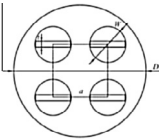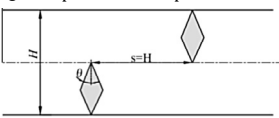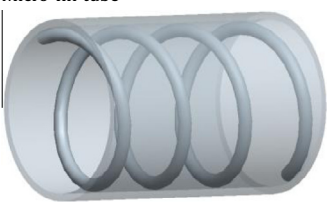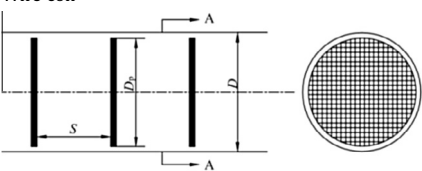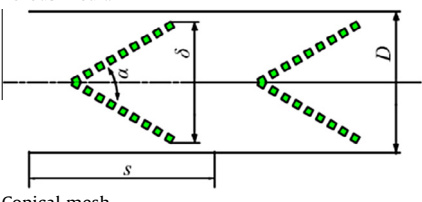
Fig. 17. Flow and temperature fields for $PPI = 200$ and 400 with $Re = 1100$, $\delta/D = 0.8$ and $S/D = 2$.

Correspondingly, thermal boundary layer is further thinned (see Fig. 17(d)). This is the reason why large PPI mesh insert should be adapted to the higher Re case.

We compared our present study with other studies in the literature. As mentioned in the Introduction section, various inserts have been investigated in the literature. Some of them have practical applications. The tube inserts include quadruple twisted tapes [21], baffle [23], internal extended surface tube with twisted tape [26], micro fins [27], wire coil [28] and porous media [29]. Table 3 lists some of the heat transfer enhancement techniques in the literature. The insert configuration, working fluid, boundary condition, EF, PEC, working principle and comments on these techniques are shown column by column. The working principle was to limit the hydraulic and/or thermal boundary layer development [27], introduce the vortex structure [23], induce the disturbance on the flow field [26,28]. Refs. [21,29] used the field synergy principle to analyze and optimize the heat transfer enhancement techniques. References [27] reported both lower EF and PEC, which covered the range of $EF = 1.06$–1.12 and $PEC = 1.0$–1.03, respectively. Reference [28] obtained moderate EF and PEC. Refs. [23,29] reported higher EF of about 5–6, but PEC values are low such as 1.1 to 1.4. Our present work had $EF = 1.4$–4.1 and

Table 3
The comparison between our present study and others in the literature.

References	Configuration	Working fluid and condition	Performance	Working principle	Comments
Zhang et al. [21]	 Quadruple twisted tapes	Air, T_w = constant $300 \leqslant Re \leqslant 1800$	EF = 2.2–3.4 PEC = 1.64–2.46	The core flow heat transfer enhancement principle	Nu is higher than that of the single twisted tapes. The pitch between two tape (a) has effects on the performance
Sripattanapipat and Promvonge [23]	 Baffle	Air, T_w = constant $100 \leqslant Re \leqslant 600$	EF = 1.1–6.5 PEC = 0.55–1.1	The baffle induces vortex, which enhances fluid mixing	The use of 5° diamond baffle performs much better than that of other baffles for heat transfer enhancement
Liao and Xin [26]	 Internal extended surface tube with twisted tape	Water, oil and ethylene glycol, $80 \leqslant Re \leqslant 2200$ q_w = constant	EF = 2.0–3.5 PEC = 1.64–2.46	Fluid mixing is enhanced by swirls induced by twisted tape, and the boundary layer is disrupted by roughness on wall	The hybrid heat transfer enhancement technique of internal extended surface tube with twisted tape is suitable for enhancing heat transfer for highly viscous fluid laminar flow
Al-Fahed et al. [27]	 Micro-fin tube	Oil, T_w = constant $300 \leqslant Re \leqslant 2200$	EF = 1.06–1.12 PEC = 1.0–1.03	The boundary layer disruption	High micro fins have significant influence on performance, which should be larger than boundary layer thickness
Akhavan-Behabadi et al. [28]	 Wire coil	Oil, T_w = constant $100 \leqslant Re \leqslant 1500$	EF = 1.8–3.2 PEC = 1.05–2.3	The flow is disturbed and the mixing between bulk and boundary layer is enhanced	Wire coil inserts with lower wire diameters have better performance. Increase of coil pitch worsens the performance
Huang et al. [29]	 Porous media	Air, q_w = constant $1000 \leqslant Re \leqslant 2200$	EF = 3.2–5.5 PEC = 1.1 1.45	Field synergy principle	The tube with porous media performs the best in laminar flow region
Present paper	 Conical mesh	Water, q_w = constant $100 \leqslant Re \leqslant 1500$	EF = 1.4–4.1 PEC = 1.2–2.2	Flow and temperature field are modulated effectively, with larger velocity near the wall and smaller in the core region	The larger δ/D and smaller S/D are, the better performance of tube will be. It is better to use low PPI mesh insert at low Re

PEC = 1.2–2.2, approaching the values reported in Refs. [21,26]. MHTT of this study had the maximum δ/D of 0.8. The heat transfer enhancement ratios will be increased by further raising the parameter δ/D. Future work should be continued on the optimization of the MHTT.

Finally, we paid attention to the possible blockage of the mesh screens. For large Reynolds number, it is recommended to use high PPI mesh screen. This involved very small mesh pore size. For example, the PPI = 400 mesh screen involved the pore width of 38 μm (see Table 1). The mesh holes are possible to be blocked by particles in the liquid. Thus, this invention is recommended to be used for pure working fluid situation. Liquids are not easy to

be polluted in closed fluid system, which is more convenient to use mesh inserts. When there are solid particles in the liquid, the device can still be used if repulsive forces exist between particles and the mesh screen. In the near future, we will try to modify the mesh screen with nano structure. Thus, hydrophobic mesh screen surface can be formed to decrease the flow resistance and delay the particle blockage of the mesh screen.

5. Conclusions

The following conclusions can be drawn:

- MHTT was constructed by suspending consecutive conical-mesh inserts in a tube. Short mesh insert helps to maintain high heat transfer coefficient, while inclined mesh screen surface decreases pressure drop rise penalty.
- The 3D to 2D conversion of mesh screens was performed by applying the equal equivalent diameter criterion and total flow area criterion. Numerical simulation was performed with multiscale grids linking micron scale of mesh pores with macroscale of tube.
- With $Re = 100$–1500, $S/D = 2.0$–3.0, $\delta/D = 0.6$–0.8, $PPI = 80$–400, MHTT had Nu which are 1.4–4.1 times of that in a bare tube, PECs were from 1.2 to 2.2, demonstrating excellent heat transfer performance with low pressure drop rise penalty.
- Perfect flow field of MHTT consists of an attached hydraulic boundary layer having large velocity and its gradient on the tube wall, a weak circulating flow region upstream of the mesh insert and a weakly positive flow region downstream of the mesh insert. A thin thermal boundary layer on the tube wall can be reached to enhance heat transfer.
- The optimal parameters are $S/D = 2.0$ and $\delta/D = 0.8$. Slopes of Nu versus Re are changed while increasing Re.
- There are best matches of PPI and Re. It is better to use low PPI mesh insert at low Re. Large PPI mesh insert caused deformed streamlines, leaving a hydraulic boundary layer departure region ahead of the mesh insert to worsen the heat transfer enhancement. On the other hand, high PPI mesh insert had better performance at high Re. Low PPI mesh insert may not establish a weak circulating flow region ahead of the mesh insert.

Conflict of interest

None declared.

Acknowledgments

References

[1] Z.H. Lin, J. Wang, R.Y. Li, G.M. Cui, Enhanced Heat Transfer Technology, Chemical Industry Press, Beijing, 2006. pp. 5–6.

[2] A. Kumar, B.N. Prasad, Investigation of twisted tape inserted solar water heaters-heat transfer, friction factor and thermal performance results, Renew. Energy 19 (2000) 379–398.

[3] S. Naga Sarada, A.V. Sita Rama Raju, K. Kalyani Radha, L. Shyam Sunder, Enhancement of heat transfer using varying width twisted tape inserts, Int. J. Eng. Sci. Technol. 2 (2010) 107–118.

[4] S. Eiamsa-ard, C. Thianpong, P. Eiamsa-ard, P. Promvonge, Convective heat transfer in a circular tube with short-length twisted tape insert, Int. Commun. Heat Mass Transfer 36 (2009) 365–371.

[5] S. Eiamsa-ard, K. Wongcharee, P. Eiamsa-ard, C. Thianpong, Thermohydraulic investigation of turbulent flow through a round tube equipped with twisted tapes consisting of centre wings and alternate-axes, Exp. Therm. Fluid Sci. 34 (2010) 1151–1161.

[6] K. Wongcharee, S. Eiamsa-ard, Friction and heat transfer characteristics of laminar swirl flow through the round tubes inserted with alternate clockwise and counter-clockwise twisted-tapes, Int. Commun. Heat Mass Transfer 38 (2011) 348–352.

[7] J. Guo, A. Fan, X. Zhang, W. Liu, A numerical study on heat transfer and friction factor characteristics of laminar flow in a circular tube fitted with center-cleared twisted tape, Int. J. Therm. Sci. 50 (2011) 1263–1270.

[8] A. Garcia, P.G. Vicente, A. Viedma, Experimental study of heat transfer enhancement with wire coil inserts in laminar-transition-turbulent regimes at different Prandtl numbers, Int. J. Heat Mass Transfer 48 (2005) 4640–4651.

[9] K. Yakut, B. Sahin, The effects of vortex characteristics on performance of coiled wire turbulators used for heat transfer augmentation, Appl. Therm. Eng. 24 (2004) 2427–2438.

[10] P. Promvonge, Thermal augmentation in circular tube with twisted tape and wire coil turbulators, Energy Convers. Manage. 49 (2008) 2949–2955.

[11] P. Promvonge, Heat transfer behaviors in round tube with conical ring inserts, Energy Convers. Manage. 49 (2008) 8–15.

[12] J.M. Wu, W.Q. Tao, Numerical study on laminar convection heat transfer in a channel with longitudinal vortex generator. Part B: Parametric study of major influence factors, Int. J. Heat Mass Transfer 51 (2008) 3683–3692.

[13] P. Naphon, M. Nuchjapo, J. Kurujareon, Tube side heat transfer coefficient and friction factor characteristics of horizontal tubes with helical rib, Energy Convers. Manage. 47 (2006) 3031–3044.

[14] Z. Cao, J.L. Xu, D.L. Sun, et al., Numerical simulation of modulated heat transfer tube in laminar flow regime, Int. J. Therm. Sci. 75 (2014) 171–183.

[15] F. Xing, J. Xie, J.L. Xu, Modulated heat transfer tube with mesh cylinder inserted, Int. Commun. Heat Mass Transfer 56 (2014) 15–24.

[16] Q.C. Chen, J.L. Xu, D.L. Sun, Z. Cao, Numerical simulation of the modulated flow pattern for vertical upflows by the phase separation concept, Int. J. Multiphase Flow 56 (2013) 105–118.

[17] D.L. Sun, J.L. Xu, Q.C. Chen, Z. Cao, Numerical study of flow pattern modulation in a vertical phase separation condenser tube, Chin. Sci. Bull. 58 (2013) 1592–1598.

[18] T.M. Liou, S.H. Chen, K.C. Shih, Numerical simulation of turbulent flow field and heat transfer in a two-dimensional channel with periodic slit ribs, Int. J. Heat Mass Transfer 45 (2002) 4493–4505.

[19] J.F. Zhang, Y.L. He, W.Q. Tao, 3D numerical simulation on shell-and-tube heat exchangers with middle-overlapped helical baffles and continuous baffles– Part II: Simulation results of periodic model and comparison between continuous and noncontinuous helical baffles, Int. J. Heat Mass Transfer 52 (2009) 5381–5389.

[20] Fluent Inc., Fluent 6.3 User's Guide, 2006, pp. 1071–1073.

[21] X.Y. Zhang, Z.C. Liu, W. Liu, Numerical studies on heat transfer and flow characteristics for laminar flow in a tube with multiple regularly spaced twisted tapes, Int. J. Therm. Sci. 58 (2012) 157–167.

[22] J.F. Fan, W.K. Ding, J.F. Zhang, Y.L. He, W.Q. Tao, A performance evaluation plot of enhanced heat transfer techniques oriented for energy-saving, Int. J. Heat Mass Transfer 52 (2009) 33–44.

[23] S. Sripattanapipat, P. Promvonge, Numerical analysis of laminar heat transfer in a channel with diamond-shaped baffles, Int. Commun. Heat Mass Transfer 36 (2009) 32–38.

[24] S. Eiamsa-ard, P. Promvonge, Thermal characterization of turbulent tube flows over diamond-shaped elements in tandem, Int. J. Therm. Sci. 49 (2010) 1051–1062.

[25] A.R. Anvari, R. Lotfi, A.M. Rashidi, S. Sattari, Experimental research on heat transfer of water in tubes with conical ring inserts in transient regime, Int. Commun. Heat Mass Transfer 38 (2011) 668–671.

[26] Q. Liao, M.D. Xin, Augmentation of convective heat transfer inside tubes with three-dimensional internal surfaces and twisted-tape inserts, Chem. Eng. J. 78 (2000) 95–105.

[27] S. Al-Fahed, L.M. Chamra, W. Chakroun, Pressure drop and heat transfer comparison for both microfin tube and twisted-tape inserts in laminar flow, Exp. Therm. Fluid Sci. 18 (1999) 323–333.

[28] M.A. Akhavan-Behabadi, R. Kumar, M.R. Salimpour, R. Azimi, Pressure drop and heat transfer augmentation due to coiled wire inserts during laminar flow of oil inside a horizontal tube, Int. J. Therm. Sci. 49 (2010) 373–379.

[29] Z.F. Huang, A. Nakayama, K. Yang, C. Yang, W. Liu, Enhancing heat transfer in the core flow by using porous medium insert in a tube, Int. J. Heat Mass Transfer 53 (2010) 1164–1174.